

Temporal evolution of the Evershed flow in sunspots[★]

II. Physical properties and nature of Evershed clouds

D. Cabrera Solana¹, L.R. Bellot Rubio¹, J.M. Borrero², and J.C. del Toro Iniesta¹

¹ Instituto de Astrofísica de Andalucía, CSIC, Apdo. 3004, 18080 Granada, Spain; [dcabera,lbello,tjti]@iaa.es

² High Altitude Observatory, NCAR, 3080 Center Green Dr. CG-1, 80301, Boulder CO, USA; borrero@ucar.edu

Received 08 May 2007 / Accepted 04 September 2007

ABSTRACT

Context. Evershed clouds (ECs) represent the most conspicuous variation of the Evershed flow in sunspot penumbrae.

Aims. We determine the physical properties of ECs from high spatial and temporal resolution spectropolarimetric measurements.

Methods. The Stokes profiles of four visible and three infrared spectral lines are subject to inversions based on simple one-component models as well as more sophisticated realizations of penumbral flux tubes embedded in a static ambient field (uncombed models).

Results. According to the one-component inversions, the EC phenomenon can be understood as a perturbation of the magnetic and dynamic configuration of the penumbral filaments along which these structures move. The uncombed inversions, on the other hand, suggest that ECs are the result of enhancements in the visibility of penumbral flux tubes. We conjecture that the enhancements are caused by a perturbation of the thermodynamic properties of the tubes, rather than by changes in the vector magnetic field. The feasibility of this mechanism is investigated performing numerical experiments of thick penumbral tubes in mechanical equilibrium with a background field.

Conclusions. While the one-component inversions confirm many of the properties indicated by a simple line parameter analysis (Paper I of this series), we tend to give more credit to the results of the uncombed inversions because they take into account, at least in an approximate manner, the fine structure of the penumbra.

Key words. Sunspots – Sun: magnetic fields – Sun: photosphere

1. Introduction

Evershed clouds (ECs) are patches of enhanced Doppler signals that move in the penumbra of sunspots. Surprisingly, there exist very few measurements of their magnetic fields. Shine et al. (1994) followed the evolution of ECs using Dopplergrams and longitudinal magnetograms taken at the Swedish Vacuum Telescope on La Palma. They observed cases of ECs with weak magnetogram signals, but this result could not be interpreted unambiguously because the magnetograms were sensitive to both field strength and field inclination variations.

Cabrera Solana et al. (2007, hereafter Paper I) used simple parameters derived from visible and infrared lines to characterize the polarimetric properties of ECs. While a complete observational description was possible, the physical mechanism behind the EC phenomenon could not be studied without a more involved analysis of the measurements.

Here we determine the physical properties of ECs by means of Stokes inversions, in an attempt to shed light on their nature. Two different models are employed: one-component atmospheres, and uncombed models that take into account the fine structure of the penumbra (Sect. 3). Sections 4 and 5 describe the physical properties of the ECs and the penumbral filaments hosting them, as well as their variation across the penumbra. Based on these results, in Sect. 6 we examine different mechanisms that could explain the EC phenomenon.

2. Observations

For a complete description of the data sets the reader is referred to Paper I. Time sequences of a small portion of the center-side penumbra of AR 10781 were taken with the two polarimeters of the German Vacuum Tower Telescope (VTT) on Tenerife. The polarimeters were operated simultaneously to record the Stokes parameters of four lines at 630 nm and three lines at 1565 nm. The cadence of the scans was 3.9 min on June 30, 2005 and 2 min on July 1, 2005, when the spot was located at heliocentric angles of 43° and 35°, respectively. Fifteen ECs moving from the mid to the outer penumbra were identified as structures of enhanced Doppler velocities during the 236 min covered by the scans. Thanks to the adaptive optics system of the VTT, the spatial resolution of the infrared measurements ($\sim 0''.6$) is one of the highest ever reached in ground-based spectropolarimetry.

3. Stokes inversions

3.1. One-component models

To invert the observed Stokes profiles we first use one-component models, i.e., we assume the whole resolution element to be occupied by a single, laterally homogeneous atmosphere. It is believed that penumbrae are formed by at least two magnetic components with different field inclinations (Title et al. 1993; Solanki & Montavon 1993; Martínez Pillet 2000; Bellot Rubio et al. 2004; Bello González et al. 2005; Langhans et al. 2005; Borrero et al. 2005; Schlichenmaier et al. 2007), so the physical quantities retrieved from these inversions

Send offprint requests to: L.R. Bellot Rubio

[★] Appendices are only available in electronic form at <http://www.edpsciences.org>

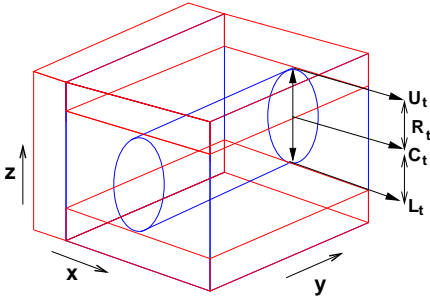


Fig. 1. Illustration of the atmospheres filling the resolution element in an uncombed penumbra. The areas enclosed by the red and blue lines represent the background and tube atmospheres, respectively. The embedded tube is characterized by its center position (C_t) and radius (R_t). U_t and L_t are the upper and lower boundaries of the tube. The y -axis is the sunspot's radial direction and z the local vertical.

must be understood as an average of the various magnetic atmospheres coexisting in the resolution element (Bellot Rubio 2003). The simplicity of the model may lead to erroneous conclusions, but it is instructive to perform such inversions to allow comparisons with earlier works.

The temperature stratification of the atmosphere is modified with 3 nodes¹. As demonstrated in Paper I, visible and IR lines display different Doppler velocities. Hence, we allow for a gradient of LOS velocity (i.e., 2 nodes) to fit all the lines simultaneously. In contrast, the magnetic field is supposed to be constant along the atmosphere. The inversion also returns height-independent macro- and micro-turbulent velocities, modeling the presence of unresolved motions. As the amount of stray light contamination is expected to depend on wavelength, the inversion code determines this contribution separately for each spectral range, which adds two more free parameters. In this way, the Stokes profiles emerging from the pixel are computed as:

$$\mathbf{I} = (1 - \alpha)\mathbf{I}_m + \alpha\mathbf{I}_{\text{stray}}, \quad (1)$$

where α is the stray light factor, $\mathbf{I}_{\text{stray}}$ the average quiet Sun intensity profile representing the stray light contribution, and \mathbf{I}_m the Stokes vector emerging from the model atmosphere. Our one-component models and those of Borrero et al. (2004) are different, since we consider height-independent magnetic fields.

The inversions are carried out using the SIR code (Ruiz Cobo & del Toro Iniesta 1992) with a total of 12 free parameters.

3.2. Uncombed models

The typical size of the fine structure of the penumbra is 150-250 km or even smaller. At the spatial resolution of our observations, atmospheres with very different properties are likely to be mixed in the resolution element. These atmospheres must be interlaced not only in the horizontal but also in the vertical direction to explain the non-zero Stokes V area asymmetries observed in visible and infrared lines. The uncombed model proposed by Solanki & Montavon (1993) incorporates

¹ Nodes are grid points of the model atmosphere where perturbations are sought. The new model atmosphere is constructed by interpolating the perturbations at the nodes to all grid points.

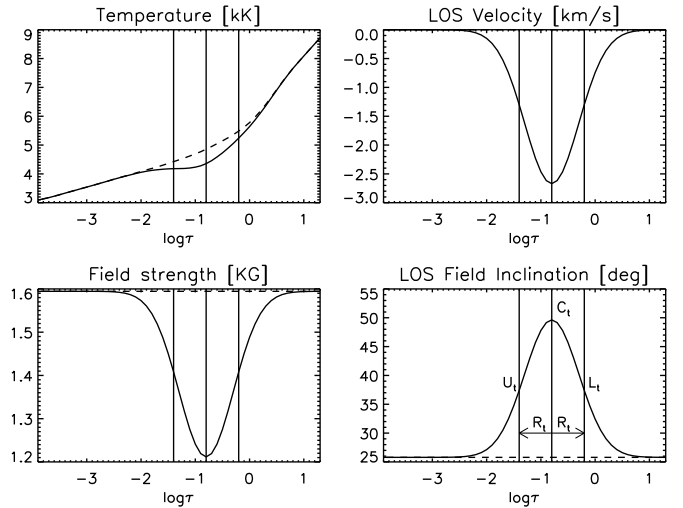


Fig. 2. Example of an initial uncombed model consisting of the background (dashed) and tube (solid) atmospheres. The gaussian is initially placed at $\log \tau = -0.8$ and has a half-width of $\Delta \log \tau = 0.5$.

the interlacing of field lines in a natural way. This model envisages the penumbra as a collection of horizontal flux tubes embedded in a more vertical background field, which agrees with the results of spectropolarimetric analyses (e.g., del Toro Iniesta et al. 2001; Schlichenmaier & Collados 2002; Bellot Rubio et al. 2004; Borrero et al. 2004, 2005, 2006; Beck 2006).

To account for the uncombed structure of the penumbra, at least to first order, the horizontal and vertical interlacing of the flux tubes and the background must be considered. To this end, we use a two-component model in which a fraction of the pixel is assumed to be filled by a background atmosphere and the rest is occupied by the background and tube atmospheres interlaced in the vertical direction (cf. Fig. 1). The emergent Stokes profiles are then the combination of the background, \mathbf{I}_b , and tube, \mathbf{I}_t , profiles:

$$\mathbf{I} = (1 - \alpha)[f\mathbf{I}_t + (1 - f)\mathbf{I}_b] + \alpha\mathbf{I}_{\text{stray}}. \quad (2)$$

The filling factor f represents the fractional area of the pixel occupied by the flux tube.

The tube atmosphere is constructed adding gaussian perturbations to the stratifications of the background component (see Fig. 2). The half-width (R_t) and position (C_t) of the gaussian are free parameters derived from the inversion and are the same for all the atmospheric parameters. In contrast, the amplitudes of the gaussian depend on the parameter. For obvious reasons, we identify R_t and C_t with the radius and central position of the tubes. Except for the temperature, the atmospheric quantities of the background are assumed to be constant with optical depth. The results of del Toro Iniesta et al. (2001), Bellot Rubio et al. (2004), and Borrero et al. (2004) demonstrate that the background atmosphere harbors much smaller velocities than the tube component, so we take the background to be at rest.

The uncombed inversions have been performed with the SIRGAUS code (Bellot Rubio 2003). This code does not account for different stray light contaminations in the different spectral ranges, but systematic errors in the determination of the stray light should produce little changes of the magnetic field properties. The number of free parameters is 17 (Table 1).

Table 1. Number of nodes employed in the uncombed inversion. -1 indicates that the two atmospheric components have the same value of the corresponding parameter.

Parameter	Background	Tube
temperature	2	1
velocity	0	1
field strength	1	1
inclination	1	1
azimuth	1	1
microturbulence	1	1
macroturbulence	-1	1
stray light	-1	1
filling factor	-1	1
gaussian position		1
gaussian width		1

3.3. Quality of the fits

As an example, Fig. 3 shows the best-fit profiles resulting from the one-component inversion of a pixel located at a normalized radial distance $r = 0.3$ (r is defined such that 0 represents the inner penumbral boundary and 1 the edge of the spot). The observed profiles are rather asymmetric, with Stokes U exhibiting four lobes. Taking into account the simplicity of the model, the match between observed and synthetic profiles is reasonably good in both spectral ranges. This suggests that the scenario adopted for the one-component inversions is appropriate to determine the ‘average’ properties of the atmosphere.

Figure 4 displays the same observed spectra and the best-fit profiles resulting from the uncombed inversion. The Stokes V area asymmetries and the shapes of Stokes Q and U are now reproduced in much greater detail. The use of the uncombed model considerably improves the quality of the fits as a result of its more realistic assumptions.

4. One-component view of the EC phenomenon

4.1. Physical properties of ECs

Figures 5 and ?? show the atmospheric parameters inferred from the inversion of the June 30 data set. The different panels display the magnetic field strength, magnetic field inclination in the local reference frame (LRF), the temperature T at $\log \tau = 0$, the LOS velocity v_{LOS} at $\log \tau = -0.5$, and the difference between the unsigned LOS velocity in two different layers, $\Delta v_{\text{LOS}} = |v_{\text{LOS}}(\log \tau = -0.5)| - |v_{\text{LOS}}(\log \tau = 0)|$. This last quantity is proportional to the gradient of velocity with optical depth.

The vector magnetic field displays the typical behavior observed in sunspots: it is weaker and more horizontal as the radial distance increases. It does not drop to zero outside the visible border of the spot, which is the signature of the sunspot magnetic canopy (Solanki et al. 1994; Westendorp Plaza et al. 2001; Rezaei et al. 2006). The ECs are visible as coherent structures with increased LOS velocity and field inclination. The presence of many moving magnetic features in the surroundings of the spot is obvious (see the arrows plotted in the first panel of Fig. ??). Their origin and nature will be discussed elsewhere (Cabrera Solana et al. 2008).

For each EC, we calculate the maximum field strength, field inclination in the LRF, and LOS velocity at $\log \tau = -0.5$ following the procedure described in Sect. 6 of Paper I. Assuming that the velocity and magnetic field vectors are aligned, the modulus of the velocity vector (*the flow velocity*) is simply

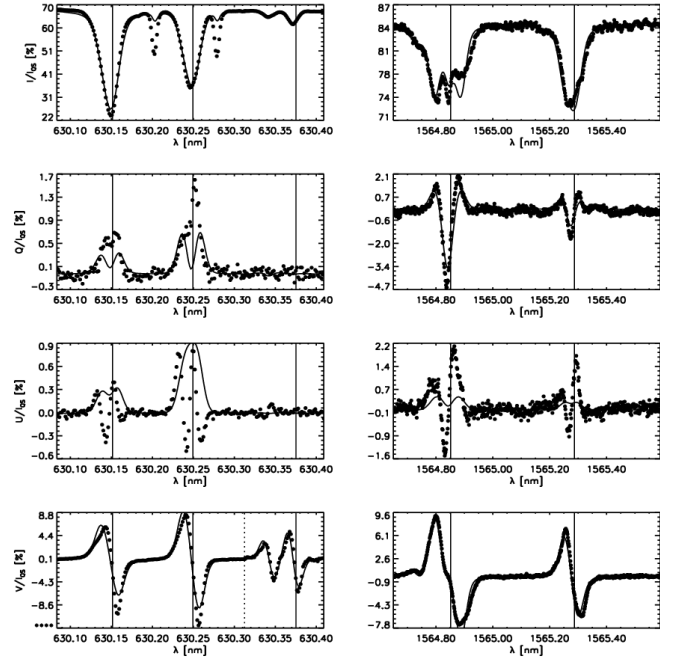


Fig. 3. Example of Stokes profiles observed at $r = 0.3$ (dots) and best-fit profiles resulting from the one-component inversions (solid lines). The O_2 telluric blends present in the visible spectra were not inverted, but they appear in the best-fit profiles due to stray light contamination. The vertical solid lines indicate the rest wavelengths of the lines. The Stokes V signal around $\text{Ti I } 630.38 \text{ nm}$ has been multiplied by six for better visibility (to the right of the vertical dotted line).

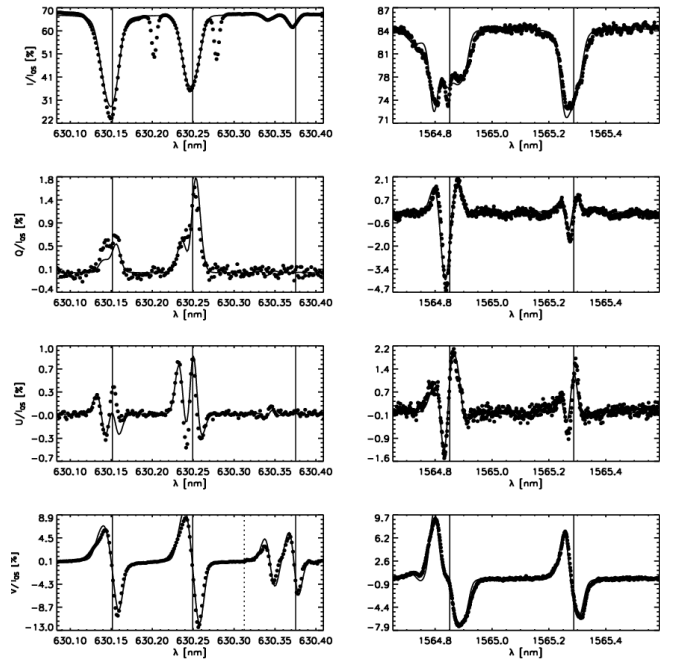


Fig. 4. Same as Fig. 3, for the uncombed inversion.

$|v| = v_{\text{LOS}} / \cos \gamma_{\text{LOS}}$. We also determine the maximum difference between the flow velocities at $\log \tau = -0.5$ and $\log \tau = 0$ ($\Delta|v|$). The results are summarized in Table 2.

The maximum field strengths attained by the ECs range from 930 G to 1070 G with an average of 1005 G on June 30, and from 1300 G to 1500 G with an average of 1408 G on July 1. In

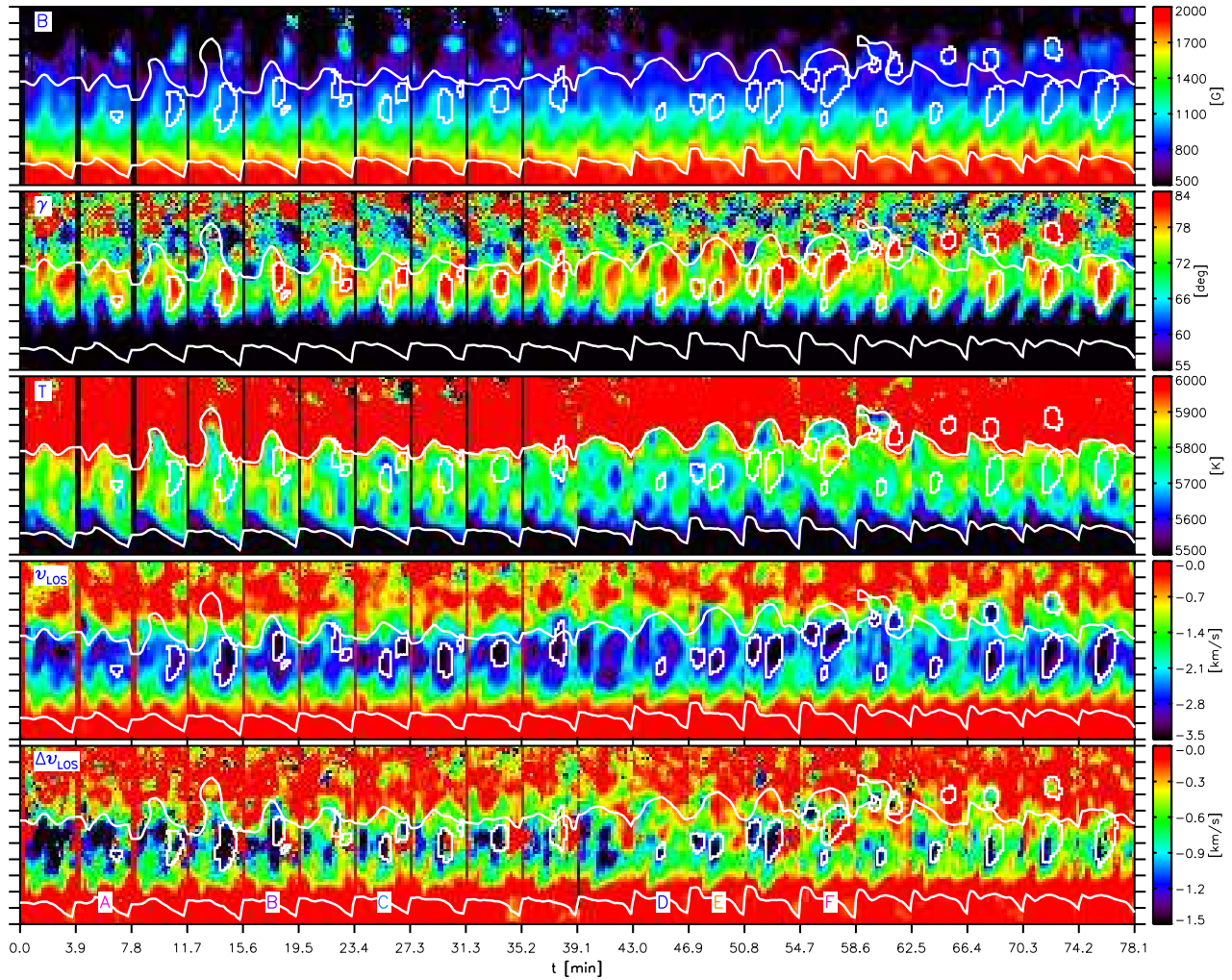


Fig. 5. *Top to bottom:* Magnetic field strength, field inclination, temperature at $\log \tau = 0$, LOS velocity at $\log \tau = -0.5$, and differences between the unsigned LOS velocities at $\log \tau = 0$ and $\log \tau = -0.5$. White contours outline the ECs and the inner and outer penumbral boundaries. The letters at the bottom of the last panel label each EC.

Paper I we discussed the compatibility of the linear-to-circular polarization ratios and LOS velocities with an scenario where the magnetic and velocity fields of the ECs are nearly horizontal to the solar surface. Table 2 confirms the existence of very inclined magnetic fields in the ECs: the average field inclination is deduced to be of the order of 82° for the June 30 observations and 71° for the July 1 data set.

Both $|v|$ and $\Delta|v|$ display higher values on June 30, i.e. when the spot is farther from disk center. The values of $|v|$ are around 4.5 km s^{-1} and 2.6 km s^{-1} on June 30 and July 1, while $\Delta|v|$ is about -0.8 km s^{-1} and -0.3 km s^{-1} on June 30 and July 1, respectively. The changes in $|v|$ and $\Delta|v|$ cannot be explained by LOS effects. Thus, the properties of the spot seem to have varied between the two observations.

4.2. Radial variation of the physical properties of ECs

The variation with radial distance of the atmospheric parameters derived from the one-component inversion is studied in this section. We calculate the radial curves of Fig. 6 in the same way as described in Paper I. The comparison of the physical proper-

ties of the ECs and the penumbral filaments hosting them (*intra-spines*, according to Paper I) shows that:

- On average, the magnetic field of the ECs is weaker than that of the intra-spines from the inner to the mid penumbra, but stronger in the outer penumbra.
- ECs harbor more inclined fields than the intra-spines at all radial distances.
- The azimuth of the field in the ECs is very similar to that found in the intra-spines at all radial distances, except perhaps in the outer penumbra.
- The flow velocity inside the ECs is greater than in the intra-spines at all radial distances.
- ECs display stronger gradients of the flow velocity with optical depth than the intra-spines.
- ECs are slightly hotter than the intra-spines in the inner penumbra, but cooler from the mid to the outer penumbra.

Therefore, in terms of one-component models, the magnetic, dynamic and thermal properties of the ECs are rather different from those of the intra-spines along which they move.

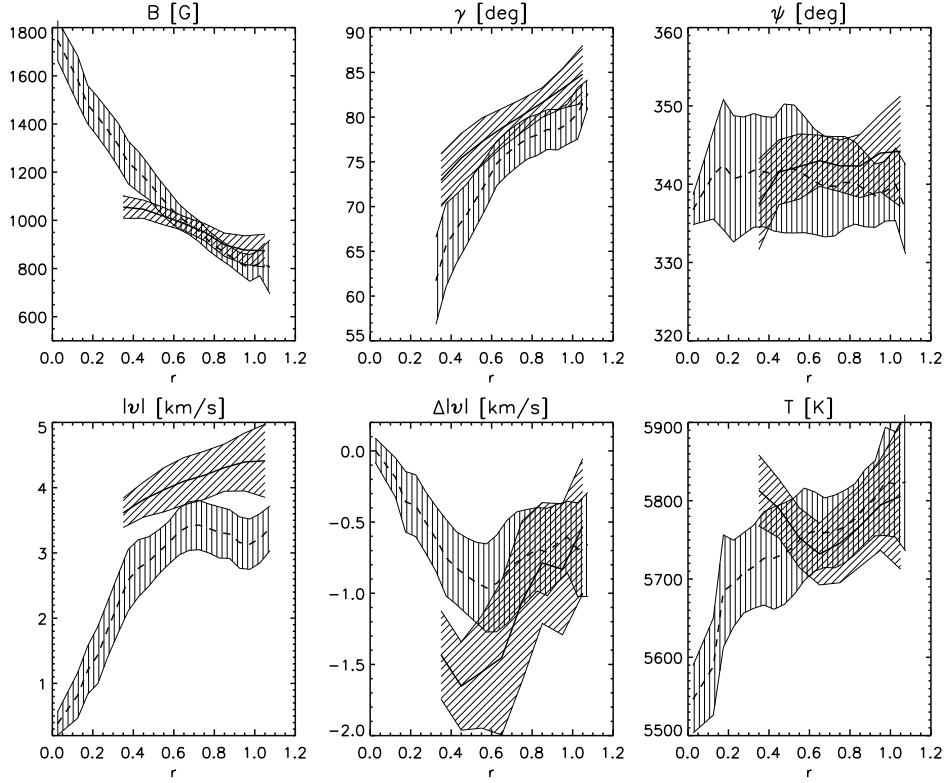


Fig. 6. Radial variation of the magnetic field strength, inclination in the LRF, azimuth, flow velocity, $\Delta|v|$, and temperature for the ECs (solid lines) and the intra-spines along which they move (dashed lines), as inferred from the one-component inversions. Shaded areas indicate the rms fluctuations of the parameters. $r = 0$ represents the inner penumbral boundary and $r = 1$ the outer edge of the penumbra

Table 2. Physical properties of the observed ECs: field strength, inclination in the LRF, flow velocity at $\log \tau = -0.5$, and the difference between the flow velocities at $\log \tau = -0.5$ and $\log \tau = 0$. Errors represent the rms fluctuations of the physical parameters within each EC.

EC	B [G]	γ [deg]	$ v $ [km/s]	$\Delta v $ [km/s]
A	1020 ± 20	81 ± 3	4.5 ± 0.4	-1.0 ± 0.6
B	1010 ± 20	83 ± 2	5.0 ± 0.5	-0.6 ± 0.4
C	1050 ± 60	80 ± 3	4.5 ± 0.3	-0.8 ± 0.6
D	1010 ± 50	82 ± 5	4.5 ± 0.8	-0.6 ± 0.6
E	980 ± 30	81 ± 3	4.2 ± 0.5	-1.1 ± 0.8
F	1070 ± 60	88 ± 5	4.8 ± 0.8	-0.4 ± 0.4
G	1010 ± 50	84 ± 2	4.2 ± 0.4	-0.6 ± 0.2
H	950 ± 40	83 ± 1	4.7 ± 0.3	-0.3 ± 0.2
I	1000 ± 50	78 ± 4	4.1 ± 0.3	-1.0 ± 0.3
J	930 ± 40	83 ± 1	4.7 ± 0.3	-0.9 ± 0.3
K	1030 ± 40	79 ± 2	4.3 ± 0.3	-1.3 ± 0.1
Mean	1005	82	4.5	-0.8
L	1470 ± 20	60 ± 3	1.4 ± 0.5	-0.2 ± 0.1
M	1440 ± 70	73 ± 3	2.5 ± 0.5	-0.2 ± 0.1
N	1430 ± 110	77 ± 2	3.1 ± 0.4	-0.3 ± 0.1
O	1290 ± 30	75 ± 4	3.2 ± 0.2	-0.2 ± 0.1
Mean	1408	71	2.6	-0.2

4.3. ECs as perturbations propagating along intra-spines

In Paper I we found that ECs exhibit larger linear polarization signals than the filaments hosting them. This led us to suggest

that they possess more inclined magnetic fields to the LOS. If the magnetic field and the velocity vectors are parallel, any increase in the LOS inclination would result in smaller LOS velocities. Thus, one has to conclude that the large Doppler signals associated with the ECs can only be produced by an increase in the modulus of the velocity vector, i.e., by stronger Evershed flows.

The maps of field inclinations and velocities displayed in Fig. 7 for EC A demonstrate that this interpretation is correct. The strong linear polarization signals seen in the EC are indeed produced by larger field inclinations to the LOS (upper left panel), which come from more horizontal fields (lower left panel). The higher LOS velocities detected in the EC are the observed signatures of stronger Evershed flows (lower right panel).

During their journey to the outer penumbral boundary, the ECs modify the magnetic field of the intra-spines along which they move, making it more horizontal locally. After the passage of an EC, the intra-spine recovers its original field inclination. Figure 8 illustrates this behaviour for the case of EC A (the arrows indicate the orientation of the vector magnetic field).

In view of these results, one could define the ECs as quasi-periodic perturbations of the magnetic and velocity fields of the penumbral filaments (intra-spines) along which they move. The main properties of these perturbations are the following: (a) they produce enhancements of γ and $|v|$; (b) the amplitude of the perturbation increases as it reaches larger radial distances; (c) when the EC starts to vanish, the amplitude of the perturbation is reduced; and (d) the modification of γ is perpendicular to the direction of propagation of the perturbation (the vertical component of the EC proper motions is small compared with the horizontal

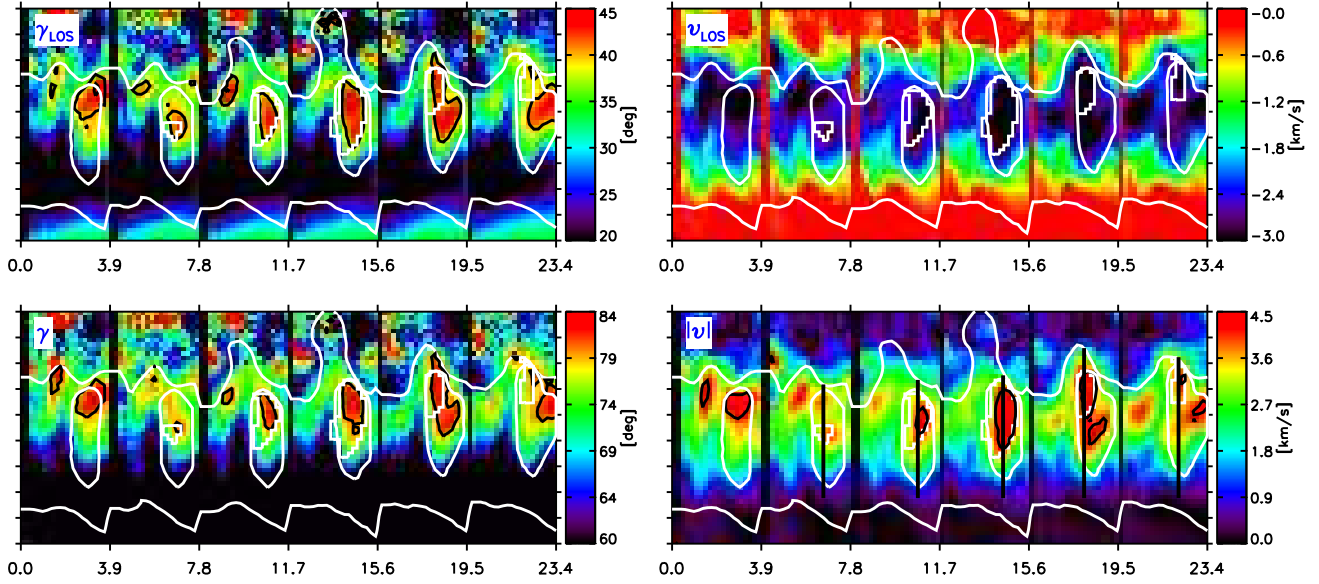


Fig. 7. *Left:* Maps of magnetic field inclination in the LOS reference frame (*top*) and the LRF (*bottom*). *Right:* Maps of LOS velocities at $\log \tau = -0.5$ (*top*) and flow velocity at $\log \tau = -0.5$ (*bottom*). White contours mark EC A, the intra-spine hosting it, and the boundaries of the penumbra. Black contours enclose pixels with γ , γ_{LOS} , and $|v|$ greater than 80° , 40° , and 4.2 km s^{-1} respectively. Each tickmark in the y -axis represents $1''$.

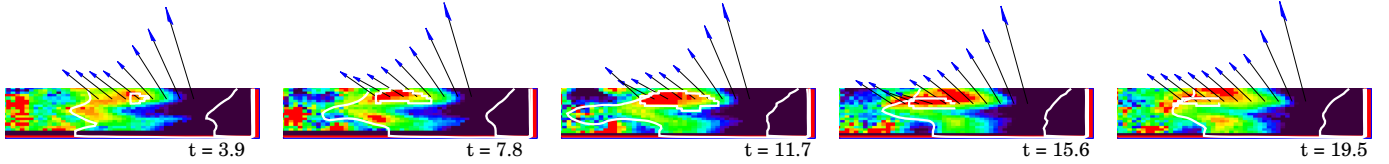


Fig. 8. Variation of γ along the cuts shown in Fig. 7 as EC A propagates from the inner ($t = 3.9$ min) to the outer ($t = 19.5$ min) penumbra. The color scale ranges from 55° (black) to 85° (red). Each arrow has the same length and indicates the orientation of the magnetic field vector retrieved from the inversion. White contours outline EC A and the penumbral boundaries.

component, cf. Paper I). Except for (c), the behavior described in this section is also observed in other type I ECs.

5. Uncombed view of the EC phenomenon

The spine/intra-spine organization of the penumbra deduced from one-component inversions can be interpreted as the azimuthal variation of the filling factors of two components whose properties remain relatively constant at a given radial distance (Bellot Rubio et al. 2004). Thus, the question naturally arises as to whether the more inclined fields and larger flow velocities of the ECs indicated by the one-component inversions are real or an artifact of simplistic modeling.

Figures 9 and ?? show the physical properties of the tube component derived from the uncombed inversions, for the June 30 data set. They already make it clear that the properties of the tubes in the ECs and the intra-spines are similar, except for the filling factor. In other words: when the fine structure of the penumbra is considered, the ECs and the intra-spines do not seem to have different physical properties. This is in contrast with the results of one-component inversions (Figs. 5 and ??).

5.1. Properties of the tube and background atmospheres inside the ECs

Figure 10 displays the radial variation of the field strength, LRF inclination, azimuth, flow velocity, temperature at $\log \tau = 0$, and filling factor of the tube and background atmospheres in the ECs. Similar curves are obtained from classical two-component inversions of the spectra (Cabrera Solana 2007), the only difference being the weaker background fields indicated by the uncombed inversions².

As expected, the field is more inclined in the tubes than in the background at all radial distances. In agreement with previous investigations (Westendorp Plaza et al. 1997, 2001; Schlichenmaier & Schmidt 2000; Mathew et al. 2003; Bellot Rubio et al. 2004; Borrero et al. 2004, 2005, 2006), field lines diving back to the solar interior ($\gamma_i > 90^\circ$) are found in the outer penumbra at the position of the ECs. The tube and background fields show differences in azimuth, but they are usually smaller than 20° .

Figure 10 demonstrates that the flow velocity increases monotonically with radial distance within the tubes, varying by some 0.7 km s^{-1} from the inner to the outer penumbra. The tube temperatures at $\log \tau = 0$ are smaller than those of the back-

² These weak fields may not be real but a consequence of initializing the inversion with low temperatures in the tubes.

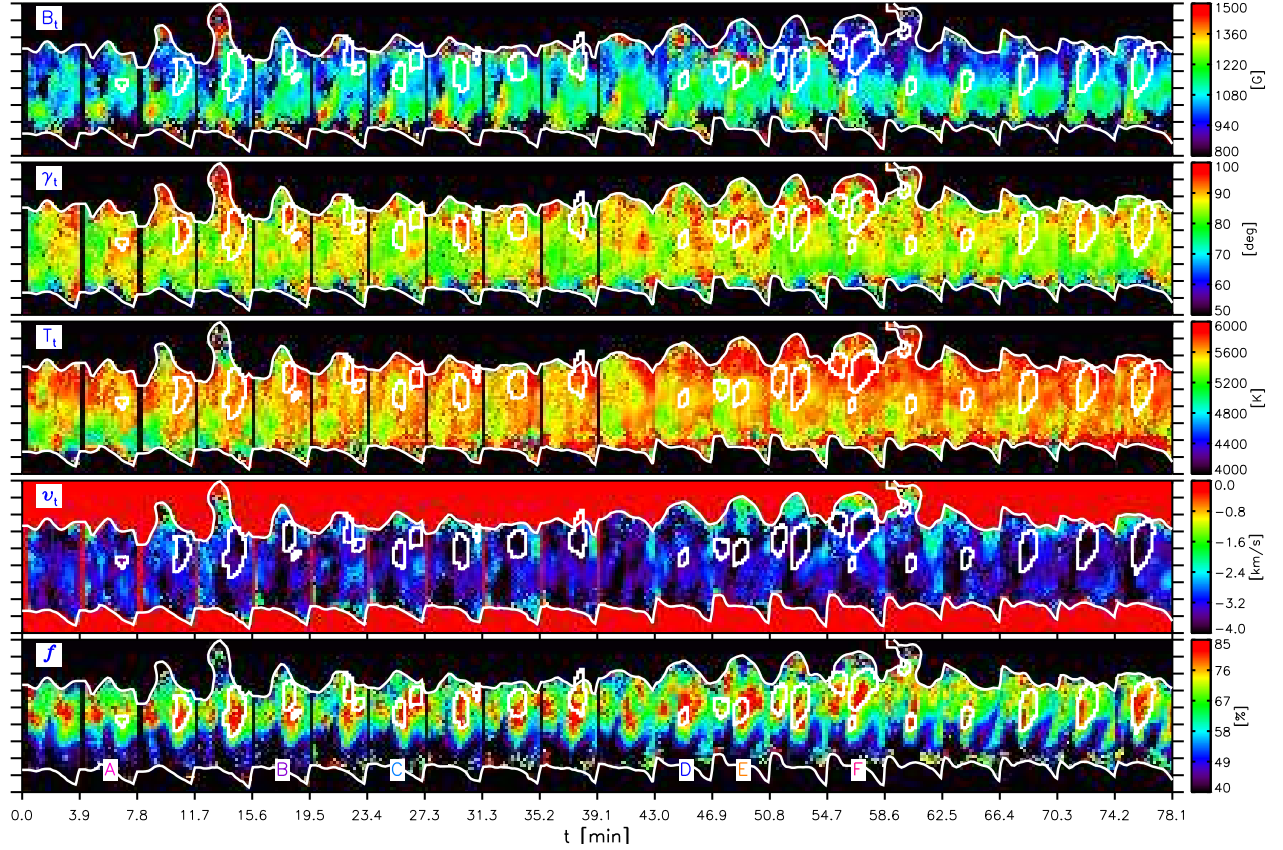


Fig. 9. *Top to bottom:* Magnetic field strength, field inclination, temperature at $\log \tau = 0$, LOS velocity, and filling factor of the tube atmosphere retrieved from the uncombed inversion. The parameters of the tubes are constructed taking the values at the tube center. White contours outline the ECs and the inner and outer penumbral boundaries. The letters at the bottom of the last panel label each EC.

ground at all radial distances. The same behavior has been found by Borrero et al. (2005, 2006), but only in the outer penumbra. The tube filling factor increases monotonically with radial distance, in agreement with Borrero et al. (2005).

5.2. Position and width of the tubes

Figure 11 examines the center position, radius, and boundaries of the tubes deduced from the inversion. At all radial distances, the tube axes are located above $\log \tau \sim 0$, with similar values in the ECs and the intra-spines. Within the scatter we do not detect differences between the ECs and the intra-spines in terms of width or position of the tube's upper boundary. The lower boundary is always below the line forming region, so the tubes are necessarily optically thick and/or low lying. This implies that the spectral lines only sample their upper halves. A similar result has been reported by Borrero et al. (2006) from uncombed inversions of penumbral profiles.

5.3. ECs as structures of increased filling factor and flow velocity

Figure 12 shows maps of the filling factor of the tube (f) as derived from the uncombed inversions (only the case of EC A is considered; the other ECs behave in a similar way). The maps clearly demonstrate that *ECs are regions of increased filling factors*. The same conclusion can be drawn from the left panel of

Fig. 13, where we plot the radial variation of f for EC A and the rest of the intra-spine. The flow velocity is also higher in the EC (right panel of Fig. 13).

The mean differences between the filling factors (Δf) and flow velocities ($\Delta|v_t|$) of the ECs and the intra-spines are displayed in Fig. 14 as a function of radial distance. Δf is of the order of 10%, while $\Delta|v_t|$ reaches 0.7 km s^{-1} . Similar plots for the field strength, inclination, azimuth, and temperature differences are also presented in Fig. 14. The values of γ_t and ψ_t turn out to be remarkably similar in the ECs and the intra-spines. The same happens with B_t and T_t . This implies that the uncombed inversion no longer interprets the ECs as perturbations of the magnetic configuration of the intra-spines. Figure 15 shows the corresponding quantities for the background atmosphere: while the passage of ECs is not associated with changes of γ_b or ψ_b , we observe small decreases of B_b and slight increases of T_b in the inner penumbra.

To understand why the code returns enhanced filling factors in the ECs, Fig. 16 compares the Stokes profiles emerging from the same pixel before and during the passage of EC A (cf. the numbers marked in Fig. 12). The figure also displays the contribution of the background and tube atmospheres to the profiles. Note that (a) the EC passage increases the linear-to-circular polarization ratios mainly through an enhancement of the linear polarization signal, and (b) the linear polarization arises almost exclusively from the tube component. This combination of factors allows the code to explain the EC profiles just by increasing

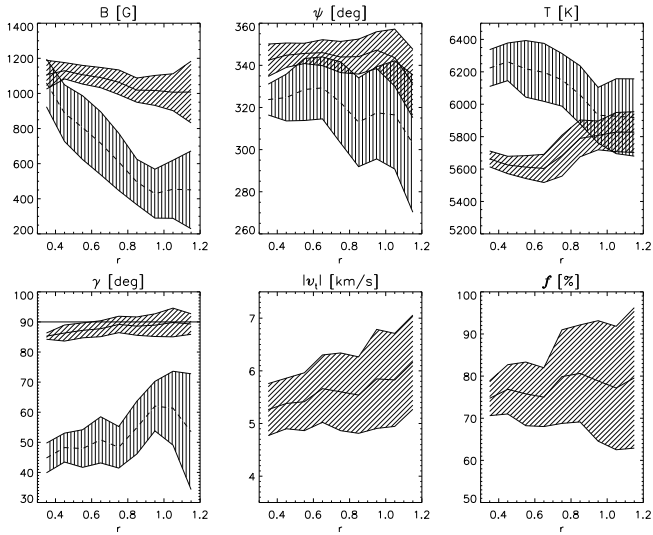


Fig. 10. Radial variation of the magnetic field strength, field inclination, field azimuth, flow velocity, temperature at $\log \tau = 0$, and filling factor of the tube (solid) and background (dashed) components within the ECs, as derived from the uncombed inversions. Shaded areas represent the rms fluctuations of the atmospheric quantities at a given distance.

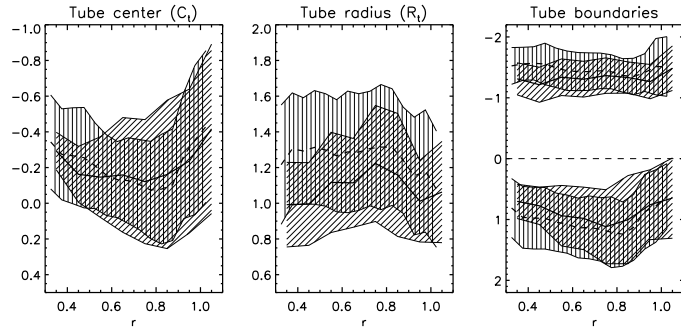


Fig. 11. Center position, radius, and boundaries of the flux tubes in the ECs (solid lines) and the intra-spines hosting them (dashed lines). The quantities are given in units of the logarithm of the optical depth. The shaded areas represent the standard deviations of the parameters.

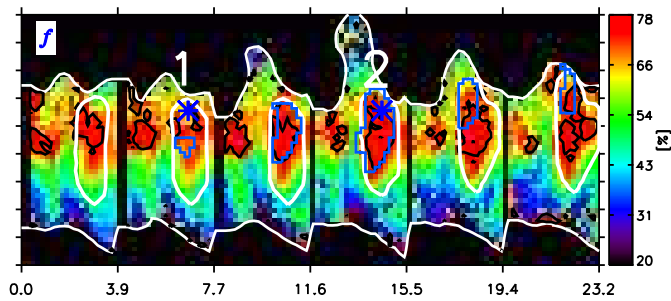


Fig. 12. Maps of the filling factor of the tube (f) derived from the uncombed inversions. White contours mark the intra-spine and the boundaries of the penumbra. EC A is outlined with blue contours. Black contours delimit pixels having f larger than 77%. Asterisks and numbers indicate the position of a pixel before and during the passage of the EC.

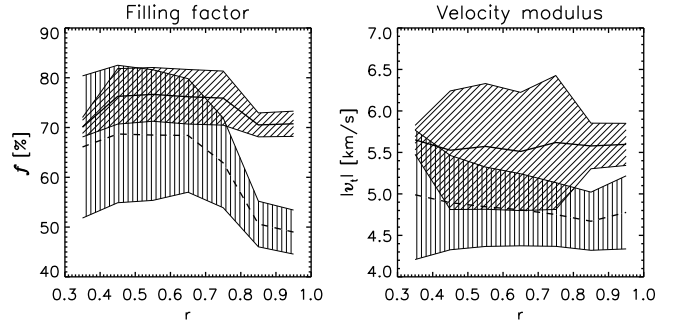


Fig. 13. Radial variation of the filling factor (left) and flow velocity (right) inside EC A (solid lines) and its intra-spine (dashed lines).

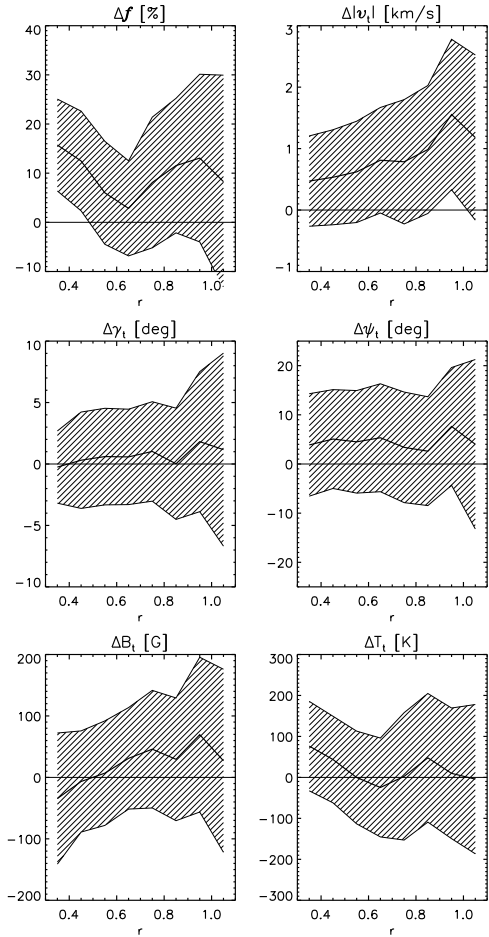


Fig. 14. Top: Differences between the filling factor (left) and flow velocity (right) of the tubes inside the ECs and the intra-spines as derived from the uncombed inversions. The shaded areas represent the rms fluctuations of the differences. Middle: Same, for the field strength and inclination. Bottom: Same, for field azimuth and temperature at $\log \tau = 0$.

the contribution of the tube atmosphere, i.e., f . In other words: the filling factors of the ECs are large as a consequence of the high linear-to-circular polarization ratios they exhibit (Paper I).

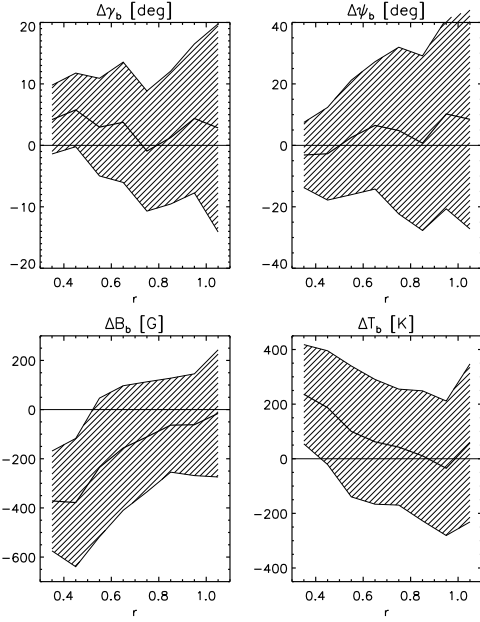


Fig. 15. Same as Fig. 14 for the field strength, inclination, azimuth, and temperatures at $\log \tau = 0$ of the background.

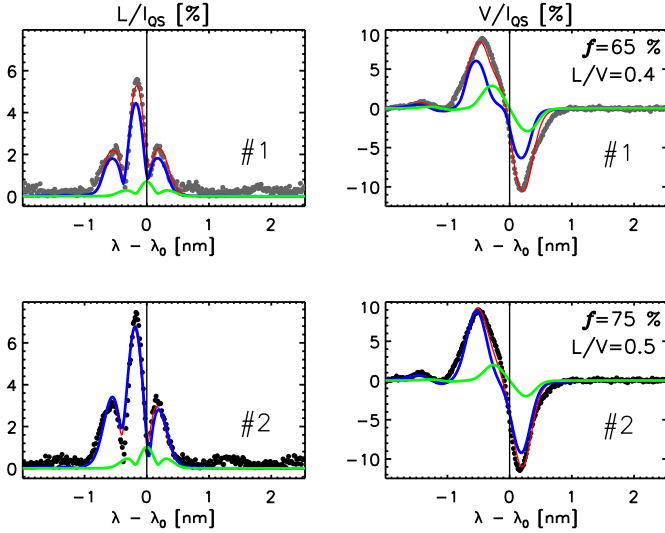


Fig. 16. Observed linear and circular polarization profiles of Fe I 1564.85 nm (dots) emerging from a pixel before (#1) and during (#2) the passage of EC A. The pixel is marked with asterisks and numbers in Fig. 12. Blue and green lines represent the contributions of the tube and background components to the best-fit profiles (red lines).

5.4. Physical origin of the increased filling factors

The large filling factors of the ECs may result from (a) an increase in the number of penumbral tubes, and/or (b) a greater fraction of the tube's cross section in the line forming region.

Option (a) seems unlikely because it would require the participation of new tubes, all of them migrating outward along intra-spines in an organized way as the ECs. Option (b) would require flux tubes with larger radii or placed higher in the photosphere. Both possibilities are ruled out by Fig. 11.

Therefore, we deem that perturbations of the thermodynamic properties of the tubes are more feasible as the source of the filling factor enhancements associated with the ECs and, consequently, as the origin of the EC phenomenon. Since no significant temperature variations occur, we suggest that the EC phenomenon is produced by *variations of density/pressure inside penumbral flux tubes*. This mechanism will be examined in Sect. 6.2.

6. Discussion

6.1. One-component interpretation

In Paper I we found that ECs are penumbral structures characterized by larger Doppler shifts, stronger linear polarization signals, and larger Stokes V area asymmetries than both spines and intra-spines. We suggested that these were observational signatures of stronger Evershed flows and more horizontal magnetic fields in the ECs as compared with the rest of the penumbra. Our one-component inversions seem to confirm this picture.

Two different mechanisms have been proposed to explain the origin of ECs: magnetoacoustic waves superimposed on a steady or quasi-steady flow (Georgakilas & Christopoulou 2003), and Ω or U kinks propagating along field lines (Ryutova et al. 1998; Rouppe van der Voort 2003). Another possibility is that ECs are the signatures of sea-serpent field lines associated with moving penumbral tubes (Schlichenmaier 2002). None of the three mechanisms seems to be compatible with the magnetic field geometry deduced from the inversions. The reason is that they should produce both an increase and a decrease of the field inclination in the ECs, but the former is not detected.

We cannot exclude that higher resolution observations may solve the problem in the future. With the present data, however, the conclusion is that origin of the magnetic field perturbations indicated by the one-component inversions remains unknown.

6.2. Uncombed interpretation

We have carried out simple numerical experiments to examine whether or not larger linear-to-circular polarization ratios and, consequently, an enhancement of f , may result from density and pressure variations inside penumbral flux tubes. To that end we use the model of flux tubes in mechanical equilibrium proposed by Borrero (2007). In this model the tubes are not thin, i.e., the physical properties change over their cross sections.

We assume two different equilibrium configurations to model the conditions of the tube and background atmospheres in intra-spines before and during the passage of an EC. In order to emulate the conditions *before* the EC passage we consider a horizontal ($\gamma_t = 90^\circ$) tube with a field strength of 1000 G that channels an Evershed flow of $|v_t| = 4.5 \text{ km s}^{-1}$. The tube is located at the heliocentric angle of the observations (43° on 30 June) with its axis pointing along the line of symmetry. It is surrounded by a background field with $\gamma_b = 60^\circ$ and $B_b = 450 \text{ G}$. The upper panels of Fig. 17 show the temperatures, gas pressures, and densities derived from the model. The x -axis is perpendicular to the tube axis and the z -axis represents the line of sight.

The only property that seems to change *during* the passage of an EC is the strength of the background field. Thus, we model the new situation using the same parameters for the tube component ($\gamma_t = 90^\circ$, $B_t = 1000 \text{ G}$, $\gamma_b = 60^\circ$) but a weaker field of $B_b = 350 \text{ G}$ in the background atmosphere. To maintain lateral pressure balance, the gas pressure and density of the tube

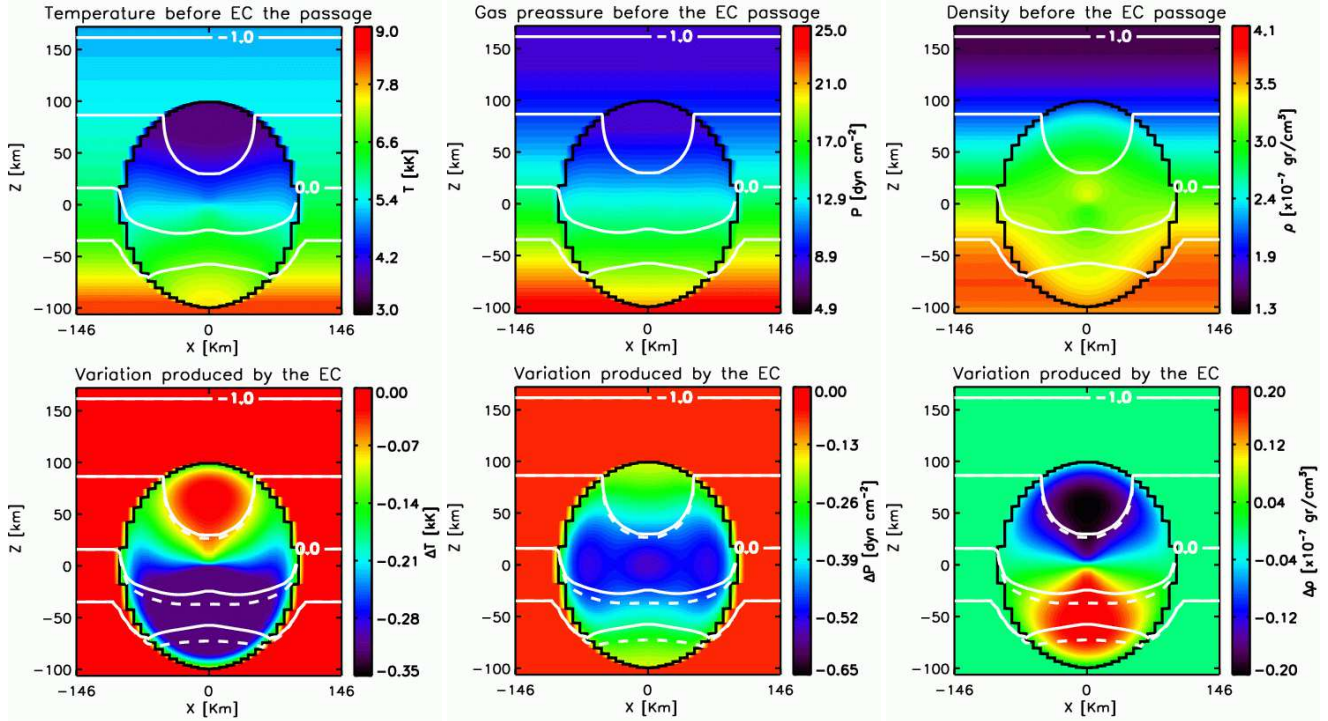


Fig. 17. *Top panels:* Temperature, gas pressure, and density in the tube and their surroundings simulating the conditions of the atmosphere before the EC passage. *Bottom panels:* Variation of the temperature, gas pressure, and density produced by the EC. The tube is enclosed by the black lines. Solid and dashed white lines indicate isocontours of optical depth ($\log \tau = -1, -0.5, 0, 0.5$) before and during the EC passage, respectively.

decrease in response to the weakening of the background field (bottom panels of Fig. 17).

The pressure and density variations associated with the EC move the optical depth scale toward deeper layers, which increases the fraction of the tube inside the line formation region (compare the solid and dashed lines in the bottom panels of Fig. 17). It is important to remark that the variation of the optical depth scale is negligible in the upper half of the tube, becoming significant only in the lower half. This may explain why the position of the tube's upper boundary is not seen to change with the EC passage.

The downward shift of the optical depth scale increases the observed L/V ratios. This is demonstrated in Fig. 18, where we show the total linear and circular polarization profiles of Fe I 1565 nm before and during the EC passage. The contributions of the tube and background atmospheres to the emergent profiles are indicated with blue and green lines, respectively. When the EC moves along the intra-spine, the linear-to-circular polarization ratio grows from $L/V = 0.22$ to $L/V = 0.27$. Since the amount of circular polarization remains roughly the same, the increase in L/V is due to an increase in the linear polarization, much in the same way as observed (Fig. 16). The larger L/V ratio is mainly due to a larger flux tube contribution. Since the magnetic properties of the tube are the same before and during the EC passage, the only possible cause is a change in the thermodynamic properties of the tube: *a decrease in the gas pressure*

*and density*³. The larger flux tube contribution is interpreted by uncombed inversions as enhancements of the filling factor.

Our experiments support the idea that the L/V increase observed during the passage of ECs is the result of lower gas pressures and densities in the penumbral tubes that carry the Evershed flow. With the model of Borrero (2007), these conditions are forced imposing a weaker external magnetic field. Such a field is consistent with the observations (Fig. 15), but its origin remains unclear.

7. Summary

In this paper we have interpreted the Stokes profiles emerging from Evershed clouds (ECs) using simple one-component and more sophisticated uncombed inversions of 4 visible and 3 infrared lines. The inversions have allowed us to determine the physical properties of ECs, the ultimate goal being to understand the nature of the EC phenomenon.

The one-component inversions confirm many of the properties indicated by the line parameter study of Paper I. The results of these inversions suggest that ECs are structures having more inclined fields and stronger Evershed flows than the rest of the penumbra. ECs move along intra-spines toward the outer boundary of the spot. In their journey, they change the magnetic configuration of the intra-spines, which only recover their initial

³ To confirm this point, we have repeated the experiment assuming that the gas pressure in the tube increases during the passage of the EC. This is induced through a larger background magnetic field ($B_b = 550$ G vs $B_b = 450$ G). As expected, the larger gas pressures and densities in the tube shift the optical depth scale toward higher layers, reducing the contribution of the tube to the linear polarization profiles and, thus, the L/V ratio.

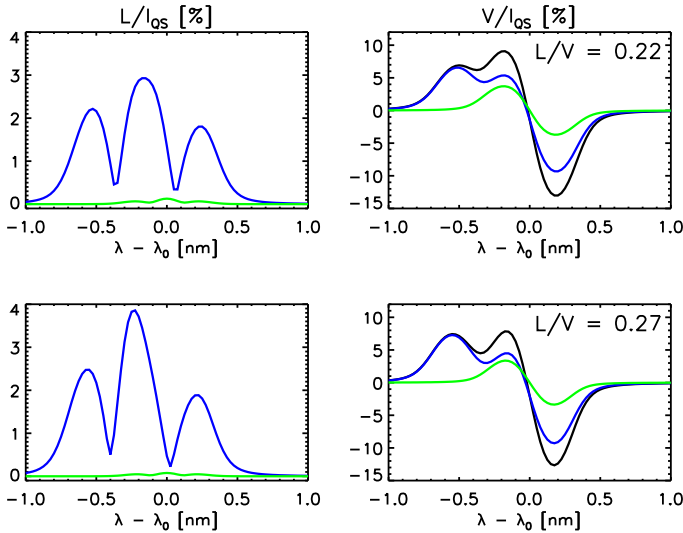


Fig. 18. Synthetic linear and circular polarization profiles of Fe I 1564.8 nm (black curves) simulating the conditions before (*top*) and during (*bottom*) the EC passage. Blue and green profiles represent the contributions of the tube and background atmospheres to the emergent profiles, respectively.

state after the passage of the ECs. Thus we suggest that the EC phenomenon is caused by a perturbation of the magnetic field of the intra-spines. None of the scenarios proposed so far for the EC phenomenon seem to be capable of explaining these findings. Both magnetoacoustic waves and magnetic kinks should give rise to vector fields pointing to the solar interior, but we do not detect them.

When we account for the fine structure of the penumbra, the EC phenomenon is no longer interpreted as a real perturbation of the magnetic field of the intra-spines. The uncombed inversions suggest that the physical properties of the penumbral flux tubes are rather similar in the ECs and the intra-spines hosting them. The background atmospheres are also similar, except for a small decrease in the field strength and slightly larger temperatures. The only significant difference observed in the intra-spines during the passage of an EC is an enhancement of the filling factor of the tube component, i.e., a larger visibility of the flux tubes that carry the Evershed flow. The inversions indicate that the enhanced visibility is not due to changes in the position or radius of the tubes. We therefore propose that the EC phenomenon is the result of variations of gas pressure and density in the flux tubes. Such variations would propagate toward the outer sunspot boundary, producing the motion of the ECs. Our interpretation is summarized in Fig. 19. Type I ECs vanish at the edge of the penumbra because the tubes return to the solar interior and the density/pressure perturbations go out of the line forming region. Type II ECs disappear in the sunspot moat (cf. Paper I), so the flux tubes associated with them have to continue well beyond the outer penumbral border (see Cabrera Solana et al. 2008).

We have performed simple numerical experiments to examine the feasibility of this scenario. We find that a decrease of the gas pressure in the upper half of the tube implies a reduction of the density, which shifts the optical depth scale toward deeper atmospheric layers. The shift does not change the optical depth of the tube's upper boundary, but makes the tube occupy a larger fraction of the line forming region. The result is an increase in the linear-to-circular polarization ratios associated with the ECs, which are interpreted by the inversion code as larger

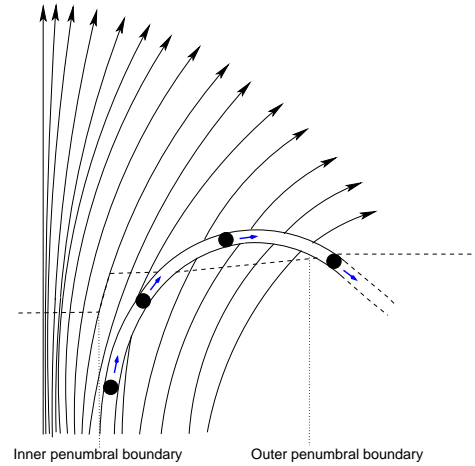


Fig. 19. Cartoon of a type I EC propagating along a penumbral flux tube which dives back to the solar interior at the outer sunspot edge. The EC is represented by the black circles. The background field is indicated by the arrows. The dashed line marks the $\tau = 1$ level, and the vertical dotted lines the penumbral boundaries. For visualization purposes, the spot is significantly compressed in the horizontal direction. This makes the flux tube appear to be elevated, but in reality it is a deep-lying tube that never reaches high photospheric layers.

filling factors. This mechanism holds promise to explain the EC phenomenon. However, further numerical and theoretical work is needed to understand the origin of the pressure/density perturbations. An interesting possibility is that they are the signatures of shocks inside penumbral flux tubes, like the ones detected by Borrero et al. (2005).

Acknowledgements. We thank P.J. Gutiérrez and D. Orozco Suárez for sharing their computing time with us. C. Westendorp Plaza generously offered his routines to plot vector fields in 3D. This work has been supported by the Spanish MEC under project ESP2006-13030-C06-02 and Programa Ramón y Cajal. The German VTT is operated by the Kiepenheuer-Institut für Sonnenphysik an the Observatorio del Teide of the Instituto de Astrofísica de Canarias. The DOT is operated by Utrecht University at the Spanish Observatorio del Roque de los Muchachos, also of the Instituto de Astrofísica de Canarias.

References

- Beck, C. 2006, Ph.D. Thesis, Alberts-Ludwig Universität, Freiburg, Germany
 Bello González, N., Okunev, O. V., Domínguez Cerdeña, I., Kneer, F., & Puschmann, K. G. 2005, *A&A*, 434, 317
 Bellot Rubio, L. R. 2003, in *ASP Conf. Ser.* 307, ed. J. Trujillo Bueno & J. Sánchez Almeida, 301
 Bellot Rubio, L. R., Balthasar, H., & Collados, M. 2004, *A&A*, 427, 319
 Borrero, J. M. 2007, *A&A*, in press, arXiv: 0704.3219
 Borrero, J. M., Lagg, A., Solanki, S. K., & Collados, M. 2005, *A&A*, 436, 333
 Borrero, J. M., Solanki, S. K., Bellot Rubio, L. R., Lagg, A., & Mathew, S. K. 2004, *A&A*, 422, 1093
 Borrero, J. M., Solanki, S. K., Lagg, A., Socas-Navarro, H., & Lites, B. 2006, *A&A*, 450, 383
 Cabrera Solana, D. 2007, Ph.D. Thesis, University of Granada, Spain
 Cabrera Solana, D., Bellot Rubio, L. R., Beck, C., & del Toro Iniesta, J. C. 2007, *A&A*, in press
 Cabrera Solana, D., Bellot Rubio, L. R., Beck, C., & del Toro Iniesta, J. C. 2008, *A&A*, in preparation
 del Toro Iniesta, J. C., Bellot Rubio, L. R., & Collados, M. 2001, *ApJ*, 549, L139
 Georgakilas, A. A. & Christopoulou, E. B. 2003, *ApJ*, 584, 509
 Langhans, K., Scharmer, G. B., Kiselman, D., Löfdahl, M. G., & Berger, T. E. 2005, *A&A*, 436, 1087
 Martínez Pillet, V. 2000, *A&A*, 361, 734
 Mathew, S. K., Lagg, A., Solanki, S. K., et al. 2003, *A&A*, 410, 695
 Rezaei, R., Schlichenmaier, R., Beck, C., & Bellot Rubio, L. R. 2006, *A&A*, 454, 975

- Roupe van der Voort, L. H. M. 2003, *A&A*, 397, 757
- Ruiz Cobo, B. & del Toro Iniesta, J. C. 1992, *ApJ*, 398, 375
- Ryutova, M., Shine, R., Title, A., & Sakai, J. I. 1998, *ApJ*, 492, 402
- Schlichenmaier, R. 2002, *Astronomische Nachrichten*, 323, 303
- Schlichenmaier, R. & Collados, M. 2002, *A&A*, 381, 668
- Schlichenmaier, R., Müller, D. A. N., & Beck, C. 2007, in Proceedings of the workshop "Modern Solar Facilities - Advanced Solar Science", ed. F. Kneer, K. Puschmann, & A. Wittmann, in press [arxiv: astro-ph/0703021]
- Schlichenmaier, R. & Schmidt, W. 2000, *A&A*, 358, 1122
- Shine, R. A., Title, A. M., Tarbell, T. D., et al. 1994, *ApJ*, 430, 413
- Solanki, S. K. & Montavon, C. A. P. 1993, *A&A*, 275, 283
- Solanki, S. K., Montavon, C. A. P., & Livingston, W. 1994, *A&A*, 283, 221
- Title, A. M., Frank, Z. A., Shine, R. A., et al. 1993, *ApJ*, 403, 780
- Westendorp Plaza, C., del Toro Iniesta, J. C., Ruiz Cobo, B., et al. 1997, *Nature*, 389, 47
- Westendorp Plaza, C., del Toro Iniesta, J. C., Ruiz Cobo, B., et al. 2001, *ApJ*, 547, 1130